AIAA JOURNAL
Vol. 36, No. 3, March 1998

Model for Rotor Tip Vortex–Airframe Interaction Part 3: Viscous Flow on Airframe

H. Affes*
Ford Motor Company, Dearborn, Michigan 48121
Z. Xiao† and A. T. Conlisk‡
Ohio State University, Columbus, Ohio 43210-1107
and
J. M. Kim§ and N. M. Komerath¶
Georgia Institute of Technology, Atlanta, Georgia 30332-0150

The behavior of vortex systems in the vicinity of solid surfaces is a matter of intense interest in rotorcraft aerodynamics, as well as in many other areas of fluid dynamics. We consider the viscous flow on a simplified model of a helicopter airframe due to a helicopter rotor tip vortex both experimentally and computationally. As the tip vortex approaches the airframe, the computational results predict the genesis of a region just upstream of the main vortex, characterized by reversed flow and rapid growth in size. The experiments clearly show evidence of such a region under the tip vortex in the region predicted by the computations and at roughly the same time. The secondary vorticity field in the computations is of a sign opposite to the vorticity associated with the tip vortex. Results for the streamline patterns and vorticity field during the genesis of the secondary eddy are presented and compared with experimental flow visualization results.

I. Introduction

THE interaction of vortices with solid boundaries is important in the study of impinging shear and mixing layers, in the study of the wakes of low-flying aircraft, in the flow within gas turbines, in the dynamic stall process, and in the study of the induced load on the fuselage of a helicopter, among many other areas. In particular, in the rotorcraft area, it has been recognized that many different interactions between many different components of the helicopter can adversely affect performance.[1] The present work is concerned with the viscous flow due to the impingement of a rotor-tip vortex on an airframe. Both experimental and computational results for the three-dimensional viscous flow on the cylindrical airframe are presented. This is the third part of a series of papers on vortex/surface interaction.[2,3]

The objective is to identify and understand the primary features of the viscous flow on the airframe due to the impinging tip vortex. However, the difficulties associated with such a study are severe; it is well known from previous work that a primary feature of boundary layers induced by vortical structures is the development of a secondary eddy in the boundary layer on the airframe, which grows in time and is eventually ejected from the boundary layer. The origin of this reversed flow, i.e., relative to the main stream velocity, begins on the subboundary-layer scale and may grow to the body scale. For the parameters of the flow of interest here, the genesis of the reversed flow region occurs on the scale of less than 1 mm and, consequently, the genesis of such a secondary structure is difficult to resolve experimentally using present-day, state-of-the-art techniques. Because the size of the secondary eddy may eventually reach body scale, a fully computational approach cannot be used to describe the full range of development because of resolution problems associated with the wide range of length scales, i.e., from 0.1 to about 70 mm. Despite the wide range of scales, the initiation of the reversed flow region may be captured both computationally and experimentally.

The experimental work reported here was carried out at Georgia Institute of Technology, and the present results are an extension of previous work to focus on the primary features of the separating boundary-layer flow. Liou et al.[4] captured the dominant features of the potential flow interaction in the plane along the top of the cylinder, and comparisons of computations with these experimental data have been reported by Affes et al.[3] That work focuses on the pressure distribution on the top of the cylinder and on the prediction of the vortex path.

In the computational work, the tip vortex is assumed to be infinitely long; this filament geometry is an idealization of the actual case where the tip vortex shed from a helicopter blade consists of a continuous helical line of concentrated vorticity. The radius of curvature of the helix is approximately the rotor blade radius, which is usually much larger than the average radius of the airframe; consequently, as the tip vortex approaches the airframe, it appears only mildly curved. The physical problem of interest is shown in Fig. 1. The three-dimensional boundary-layer problem for the case where the inviscid flow is symmetric about the y axis has been considered computationally by Affes et al.[5] and the purpose of this paper is to consider the asymmetric viscous flow on the airframe corresponding to the inviscid flow problem considered by Affes et al.,[3] Liou et al.,[4] Brand et al.,[6] and Brand.[7] The inviscid problem for the symmetric mean flow has been considered by Affes.[8] The fluid is assumed to be incompressible, inviscid, and irrotational outside the core of the vortex and away from the airframe boundary.

Affes et al.[5] have considered the fully three-dimensional unsteady problem for the case where the vortex is symmetric about the y axis of Fig. 1. The boundary-layer flow is assumed to be impulsively started. Those results show the appearance of a three-dimensional region of reversed flow, which grows in time and reaches about one-third of the boundary-layer edge in height. The eddy spans about 20 deg to either side of the top of the cylinder on Fig. 1. Complicating the situation is the emergence of a three-dimensional separation singularity, which occurs as the displacement velocity grows; this singularity is characterized by the edge velocity behaving as $v_e \sim (t_s - t)^{-7/4}$, and this behavior is confirmed by the numerical solutions.

Received April 11, 1996; revision received Aug. 1, 1996; accepted for publication Sept. 7, 1997.

*Product Design Engineer, Power Train Operations.
†Graduate Research Assistant, Department of Mechanical Engineering; currently Advanced Engineer, Combustion and Gas Turbine Department, Westinghouse Corporation, Orlando, FL 32826.
‡Professor, Department of Mechanical Engineering. Associate Fellow AIAA.
§Research Associate, School of Aerospace Engineering; currently Principal Researcher, Aerodynamics Department, Korea Aerospace Research Institute, Taejon, Republic of Korea.
¶Professor, School of Aerospace Engineering. Associate Fellow AIAA.

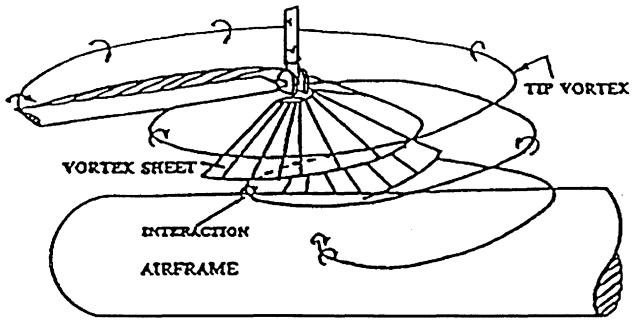

Fig. 1a Wake of a single-bladed rotor in low-speed forward flight.

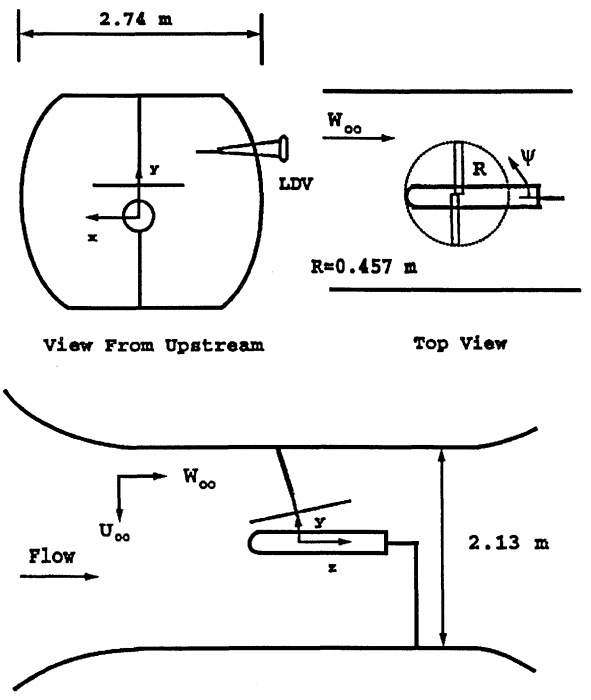

Fig. 1b Experimental configuration and coordinate system.

The vortex/boundary-layer interactions described have been observed experimentally by Harvey and Perry[9] and in the experiments described in Ref. 10. In particular, explosive boundary-layer growth and eventual ejection of a secondary vortex ring were observed to occur. Ersoy and Walker[11] and Hon and Walker[12] have computed the boundary-layer flow due to a loop vortex and a hairpin vortex, respectively, along a symmetry plane present in each case.

The purpose of the present work is to elucidate the initiation of the secondary eddy in a configuration typical of applications in the rotorcraft environment. The early stages of the development of the secondary eddy in the boundary layer under the main tip vortex have been captured both computationally and experimentally. The experimental results support the computational results and indicate the appearance of a secondary flow under the main vortex that is clearly discernible in the experiments at a rotor phase angle $\psi = 36$ deg. The rotor phase angle is defined as the angle between the advancing blade and the generators of the circular cylinder used to model the airframe (see Fig. 1).

The genesis of this secondary flow is indicated by the computations, which show a reversed flow region developing under the main vortex just prior to $\psi = 30$ deg; the vorticity in the reversed flow region is of a sign opposite to that of the main vortex and, in the computations, begins to increase rapidly just after $\psi = 30$ deg.

II. Inviscid Flow

The procedure to advance the vortex and to obtain the surface speeds is described in detail by Affes and Conlisk[2] and Affes,[8] and what follows is a short summary of that work. The vortex is advanced according to the evolution equation

$$\frac{\partial X}{\partial t}(s, t) = U \tag{1}$$

where the timescale t is defined by

$$t = (W_\infty/a)t^* \tag{2}$$

where t^* is dimensional, W_∞ is the velocity scale, and

$$U = U_I + U_V + U_M \tag{3}$$

where U_V is the velocity distribution induced by the vortex itself, U_I is the image distribution in the cylinder, and U_M is the mean flow distribution. In Eq. (1), s is a parametric value measuring distance along the vortex. The velocity U has been nondimensionalized on W_∞, and lengths have been scaled on a, which is the radius of the cylinder (0.067 m). Here W_∞ is taken to be the axial mean flow component, and the dimensionless circulation is defined by

$$\Gamma = \Gamma^*/(W_\infty a) \tag{4}$$

The initial position of the vortex is specified from experimental data as described by Affes et al.[3] The vortex-induced velocity U_V is defined by the standard Biot–Savart law[13] with a cutoff parameter based on the Rankine vortex.[11,14] We consider only the case where there is no axial flow in the vortex.

The mean flow distribution corresponds to the asymmetric distribution discussed by Affes et al.[3] Accounting for the asymmetry of the vortex geometry about the y axis is not trivial and involves the modification of the uniform flow condition at upstream ∞ in both the z and r directions, as discussed in Ref. 3.

The image of the vortex in the cylinder is calculated using the Fourier transform in the z and θ directions, and the details of this calculation is described in Ref. 3. The pressure gradients are calculated from Euler's equations in a coordinate system traveling with the head of the vortex. Let (r, θ, Z) denote the fixed polar coordinate system; then the new coordinate system, whose origin is moving with the vortex head speed U_c, is given by (r, θ, z) where

$$z = Z - Z_{Vc}(t)$$

Here, Z_{Vc} is the position of the vortex head in the z direction. The third-order upwind differencing scheme, which is used to treat the nonlinear terms in the boundary-layer equations, is also employed to compute the nonlinear terms in the Euler equations. The upwind scheme is discussed in Sec. III. Details of the calculation of the surface speeds and the pressure gradients are presented in Ref. 8.

As has been mentioned earlier, extensive experimental and analytical/computational results for the vortex evolution and for the pressure distribution on the airframe prior to vortex impact with the top of the cylinder have been presented elsewhere. The dominant interaction of the tip vortex and the boundary layer is expected to be located near the top of the cylinder, and the experimental results show that the effect of the tip vortex appears to be significant from about $\psi \sim 10$ to 72 deg for an advance ratio of 0.1 (Ref. 6). To carry out the computational work, the pressure gradients and the surface speeds from that work are required, and we discuss some of those results now. The following results are from Ref. 3.

In Fig. 2 are two views of the vortex trajectory for an advance ratio of $\mu = 0.1$, where μ is the advance ratio defined as the forward flight speed to that of the rotor tip speed. The circles denote the experimental results (not to scale for the vortex core); the times shown are for $\psi = 0$ (the initial condition), 30, and 60 deg. Here ψ is measured from the beginning of the period; in general, the absolute age of the vortex in the experiments is $\psi_{abs} = \psi + 180$ deg. The error bars correspond to about 15 mm, which is about one vortex diameter. Note the substantial agreement between theory and experiment, especially at $\psi = 30$ deg. At $\psi = 60$ deg, the vortex is about one core radius from the airframe, and some uncertainty in the precise position of the vortex near impact does exist; consequently, those

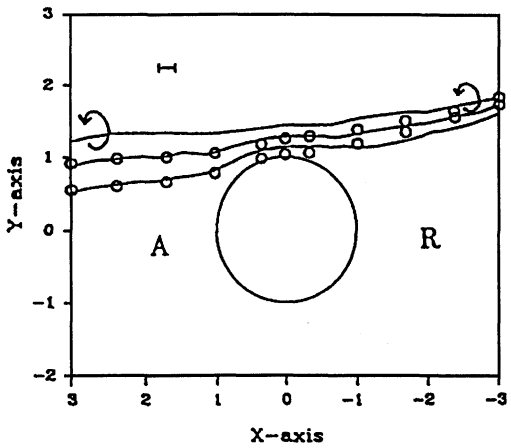

a) Upstream end view

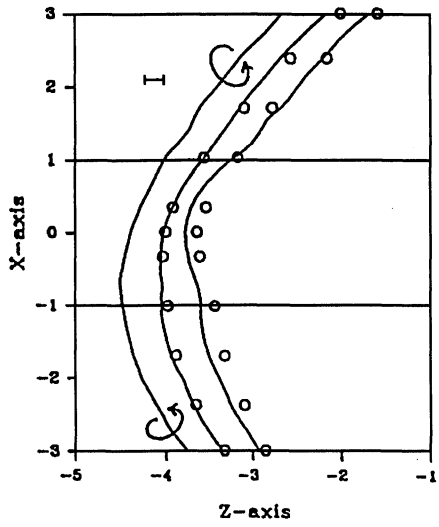

b) Top view

Fig. 2 Vortex trajectory for advance ratio $\mu = 0.1$; error bar in the experiments is shown: A, advancing side of the rotor and R, retreating side.

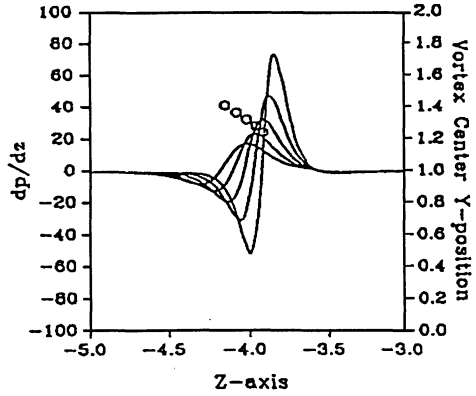

Fig. 3 Axial pressure gradient imposed on the viscous flow on the airframe at several times corresponding to ψ = 18, 24, 30, 36, and 42 deg; o, side views of the computed vortex head position.

experimental data points nearest the airframe should be viewed with caution. In Fig. 3 the time evolution of the axial pressure gradient on the top of the airframe is shown. Note the strong adverse pressure gradient that develops as the vortex approaches the airframe. Moreover, as ψ increases the pressure gradient becomes more focused locally in space; in addition, it is apparent that a short timescale is also emerging, as evidenced by the rapid increase in the amplitude of the pressure gradient from $\psi = 42$ to 54 deg.

III. Viscous Flow

The governing equations are the three-dimensional, unsteady boundary-layer equations; these equations are discussed in detail elsewhere,[5,8] and the final form of the equations is

$$\frac{\partial \tilde{u}_r}{\partial \eta} + \frac{\partial \tilde{u}_\theta}{\partial \theta} + \frac{\partial \tilde{u}_z}{\partial z} = 0 \tag{5}$$

$$4t\frac{\partial \tilde{F}}{\partial t} - 2\eta\frac{\partial \tilde{F}}{\partial \eta} - \frac{\partial^2 \tilde{F}}{\partial \eta^2} = -4tP + R \tag{6}$$

where $F = (\tilde{u}_\theta, \tilde{u}_z)$, $P = (\partial p/\partial\theta, \partial p/\partial z)$, and $R = (R_\theta, R_z)$, where

$$R_\theta = -4t\left(\frac{u_r}{2\sqrt{t}}\frac{\partial u_\theta}{\partial \eta} + u_\theta\frac{\partial u_\theta}{\partial \theta} + u_z\frac{\partial u_\theta}{\partial z}\right) \tag{7}$$

$$R_z = -4t\left(\frac{u_r}{2\sqrt{t}}\frac{\partial u_z}{\partial \eta} + u_\theta\frac{\partial u_z}{\partial \theta} + u_z\frac{\partial u_z}{\partial z}\right) \tag{8}$$

and the Rayleigh variable η is defined by $\eta = y/2\sqrt{t}$.

Equations (5) and (6) are subject to the following initial and boundary conditions: $\tilde{u}_\theta$ and $\tilde{u}_z$ specified at $t = 0$; $\tilde{u}_r$, $\tilde{u}_\theta$, and $\tilde{u}_z$ specified as $z \to \pm\infty$; $\tilde{u}_r = \tilde{u}_\theta = \tilde{u}_z = 0$ at $y = 0$; $\tilde{u}_\theta \to U_\theta - U_\theta^0$ as $y \to \infty$; $\tilde{u}_z \to U_z - U_z^0$ as $y \to \infty$; and $\tilde{u}_\theta$ and $\tilde{u}_z$ periodic in θ as $y \to \infty$; where U_z^0 and U_θ^0 are the inviscid surface speeds at $t = 0$ and U_z and U_θ are the corresponding inviscid surface speeds at subsequent times t. The velocities denoted by tildes are defined by

$$u_\theta = \tilde{u}_\theta + u_\theta^0 \tag{9}$$

$$u_z = \tilde{u}_z + u_z^0, \qquad u_r = 2\sqrt{t}(\tilde{u}_r + u_r^0) \tag{10}$$

where[2,11]

$$u_\theta^0 = U_\theta^0 \operatorname{erf}\eta, \qquad u_z^0 = U_z^0 \operatorname{erf}\eta \tag{11}$$

The dimensionless variables are defined by

$$\theta = \theta^*, \qquad z = z^*/a, \qquad y = [(r^*/a) - 1]Re^{\frac{1}{2}}, \qquad t = (W_\infty/a)t^*$$

and the velocities are scaled on W_∞. Here a is the radius of the cylinder and $Re = W_\infty a/\nu$ is the Reynolds number; the pressure p^* is nondimensionalized on ρW_∞^2.

For future reference, it is useful to investigate the induced vorticity field. Using the boundary-layer scaled variables just defined and dropping the terms of the order $(Re^{-1/2})$ the scaled vorticity field takes a simpler form and is defined by

$$Re^{-\frac{1}{2}}\omega = \omega_\theta \hat{i}_\theta + \omega_z \hat{i}_z \tag{12}$$

where ω_θ and ω_z are the azimuthal and the axial scaled vorticity components, respectively, given by

$$\omega_\theta = -\frac{1}{2\sqrt{t}}\frac{\partial u_z}{\partial \eta} \tag{13}$$

and

$$\omega_z = \frac{1}{2\sqrt{t}}\frac{\partial u_\theta}{\partial \eta} \tag{14}$$

The numerical scheme used to solve the three-dimensional boundary-layer equations is a combination of finite difference methods and Fourier transform methods; the details of the scheme are presented in detail elsewhere.[5] In the η direction, a coordinate transformation is employed to cluster the grid near the wall of the cylinder, and central finite difference formulas are applied to the resulting derivatives in the normal direction. The implicit Crank–Nicolson marching technique is employed to advance the solution in time, and the standard third-order upwind scheme is employed to discretize the viscous terms.

All of the relevant inviscid flow parameters are for the case where the advance ratio $\mu = 0.1$. The time step employed in these calculations is $\Delta t = 0.00444$, which corresponds to $\Delta\psi = 0.375$ deg. There have been tested 31, 61, and 121 grid points in η; 32, 64, and 128 grid points in θ; and 61, 121, and 241 grid points in z, and it

was found that the grid (61, 64, 121) corresponding to the direction (η, θ, z) gives at least two-digit accuracy for the finest two grids.

The axial coordinate for the viscous calculations has its origin directly under the vortex at $\theta = \pi/2$ at time $t = 0$, and the results are computed in this fixed frame of reference in contrast to the coordinate system shown in Figs. 1 and 2b. All other computational details may be found in Refs. 8 and 15.

IV. Computational Results

The response of the viscous flow on the airframe to the approach of the tip vortex is characterized by the development of a secondary eddy, whose genesis is located deep within the boundary layer about (for the parameters of the experiment) 1 mm from the airframe. The character of the secondary flow is associated with a rapidly focusing region of concentrated vorticity of sign opposite to that of the primary tip vortex. To describe the genesis of the secondary flow region, the three-dimensional streamline patterns associated with the boundary-layer flow have been calculated for several instants in time in the same way as described in Ref. 5. To compare with the experimental flow visualization results, a dimensionless circulation of $\Gamma = -2.33$ has been used. This value of the dimensionless circulation is based on an estimate of the dimensional circulation of $\Gamma^* \sim -1.5\,\mathrm{m}^2/\mathrm{s}$, which was obtained from a detailed analysis of the relevant velocity contours on the top of the airframe.[4]

Figure 4 shows streamline patterns for two times indicating the inception of a secondary eddy. The surface streamlines are also shown in Fig. 4. The second eddy is absent at $t = 0.1421$, as can be seen in Fig. 2a. The streamlines begin to kink at about $t = 0.2843$ ($\psi = 24$ deg) and by time $t = 0.3554$ ($\psi = 30$ deg), the eddy is well developed. At time $t = 0.3953$ ($\psi \sim 33.3$ deg; not shown) it encompasses about 10 deg from the vertical on each side. Note that these streamline patterns are plotted in a fixed reference frame.

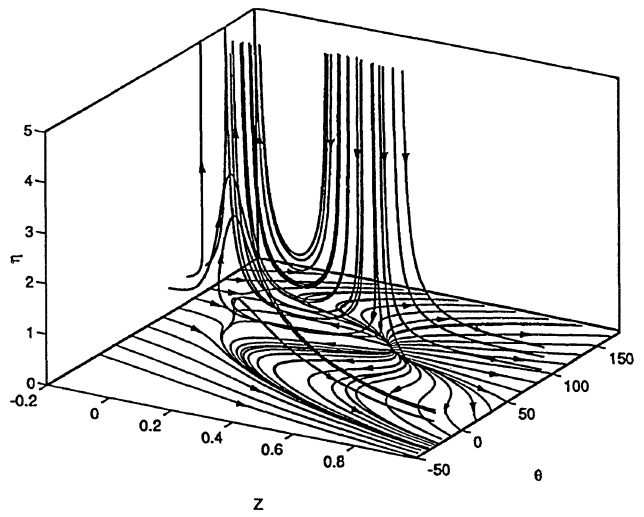

a) $t = 0.1421$ ($\psi = 12$ deg)

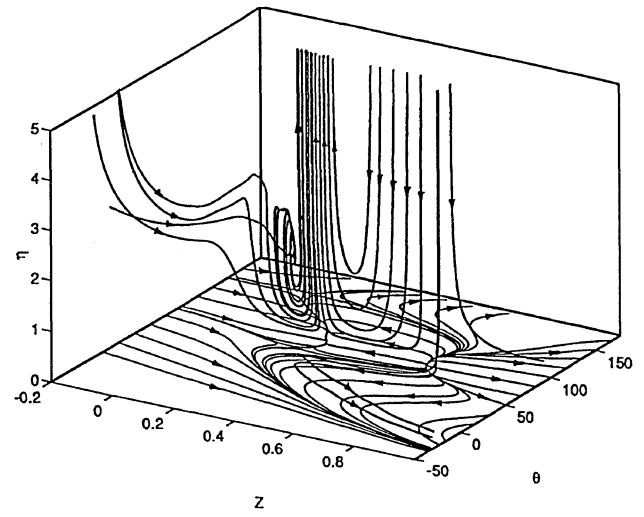

b) $t = 0.3554$ ($\psi = 30$ deg)

Fig. 4 Streamline patterns for two times in the laboratory or fixed reference frame.

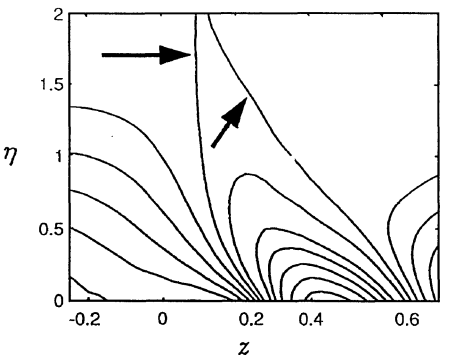

a) $\theta = 90$ deg

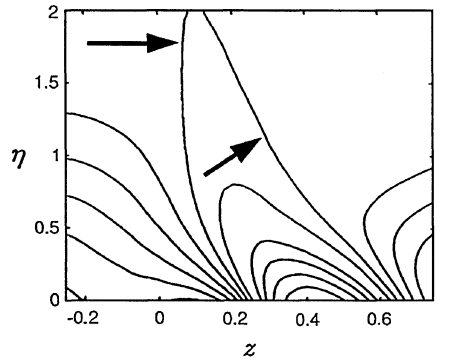

b) $\theta = 101.25$ deg

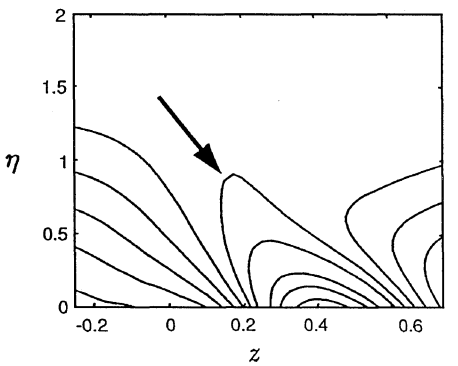

c) $\theta = 112.5$ deg

Fig. 5 Azimuthal vorticity at $t = 0.3554$ ($\psi = 30$ deg) plotted for values ranging from -1 to 3.0 in even increments.

Figure 5 shows lines of constant azimuthal vorticity ω_θ plotted at various azimuthal locations around the cylinder at the time $t = 0.3554$. The constant vorticity lines are plotted for values from -1.0 to 3.0. The increment for the positive vorticity values that occur inside the zero-vorticity line (and marked with an arrow) is 0.5 and the increment for the negative vorticity values that occur outside the zero vorticity line is 0.2. Figures 5a–5c correspond to distributions of azimuthal vorticity across the boundary layer in the planes $\theta = 90$, 101.25, and 112.5 deg, respectively. The vorticity patterns show that the region associated with positive vorticity, i.e., opposite to that of the tip vortex, diminishes in size at locations removed from the vertical plane of symmetry. At this time, the maximum value of the vorticity is not large (~ 3.0); the maximum azimuthal vorticity occurs around $\theta = 90$ deg and decreases for $\theta > 90$ deg. Note that the maximum positive vorticity shown in Figs. 5b and 5c is $\omega_\theta = 2.5$. On the other hand, at time $t = 0.3953$ the vorticity (not shown) has increased substantially to $\omega_\theta \sim 10$ near $\theta = 100$ deg indicating

the emergence of a high vorticity region off $\theta = 90$ deg on the retreating side of the rotor.

Concurrent with the rapid increase in magnitude of the vorticity field is a rapid increase in the radial velocity. Figure 6 is a three-dimensional plot of the radial velocity u_r at the edge of the boundary layer plotted around the cylinder for the time $t = 0.3554$ ($\psi = 30$ deg). Note that u_r is the edge velocity in the boundary-layer scale and $u_r = \sqrt{Re}u^*/W_\infty$. As for the symmetric flow case,[5] these results show that large variations of the radial velocity occur at locations directly under the main vortex. At points removed from the vicinity of $\theta \sim 90$ deg, the edge velocity is small, although the edge velocity seems to be larger on the retreating side of the rotor than on the advancing side at this time. This behavior is symptomatic of a subsequent eruption of fluid from the boundary layer. This eruptive region is clearly visible in the experimental flow visualization results, which will be discussed in the next section.

The azimuthal vorticity component ω_θ at $t = 0.3953$ for $\eta = 0.5$ and 1.2 off the cylinder surface is shown in Fig. 7a. We see that the azimuthal vorticity is highly concentrated in a small region near the top of the cylinder. The maximum azimuthal vorticity occurs at $z \approx 0.275$, which corresponds to the position where the boundary layer is expected to erupt into the inviscid flow region.

As with the symmetric calculations of Affes et al.,[5] a singularity is expected to emerge in the radial velocity component in a finite time. Because the variation of the flow in the cross stream (here the θ direction) is mild compared to the variation in the z direction and in the radial direction within the boundary layer, the singularity should develop as predicted by Elliott et al.,[16] who predict that $u_{r,\text{edge}}$ behaves as

$$\max(u_{r,\text{edge}}) \sim (t_s - t)^{-\frac{7}{4}} \quad \text{as} \quad t \to t_s \tag{15}$$

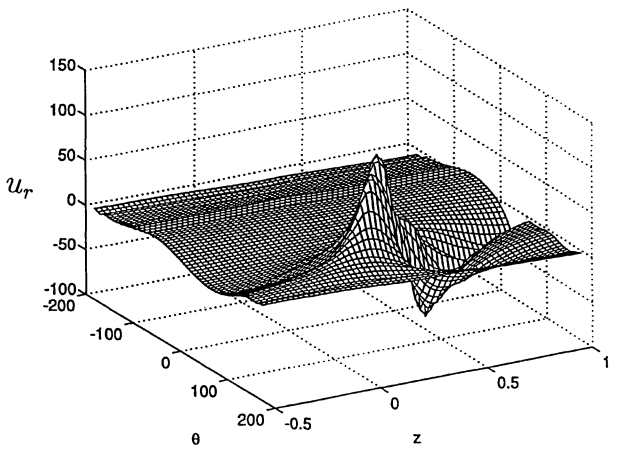

Fig. 6 Three-dimensional plot of the radial velocity around the cylinder at ψ = 30 deg; note the large spike around where the tip vortex will eventually impact the airframe.

The numerical data show that the variation of $\max(u_{r,\text{edge}})^{-4/7}$ vs t is linear in the latter stages of the calculation, and the time of the van Dommelen–Cowley[17] type singularity is predicted to be about 0.48 (about $\psi = 40$ deg). The linear curve fit of $\log[\max(u_{r,\text{edge}})]$ vs $\log(t_s - t)$ indicates that the power of $(t_s - t)$ is -1.747, which is very close to the asymptotic value $-\frac{7}{4}$. Similar results have been obtained by Affes et al.[5] The location where the maximum normal velocity occurs is at $z = 0.275$ and $\theta = 78.75$ deg.

V. Experiments

Experimental work at the Georgia Institute of Technology has continued since Liou et al.[4] captured the dominant features of the potential flow interaction in the plane along the top of the cylinder. Recent experiments have focused on the events occurring upstream of the main vortex immediately before it collides with the surface.

A pulsed copper vapor laser beam, expanded into a sheet, was used to illuminate desired vertical planes above the surface of the cylinder. This produced 6300 pulses/s, each pulse lasting for only 25–50 ns. The scattering from the light sheet was recorded using an intensified charge-coupled device video camera operating at 29.97 frames/s, each frame exposed for 100 μs. Thus, the image contains information from only one pulse of the laser, freezing the flowfield with an effective 25-ns exposure. Each frame captures 1 or 0 flashes of the laser sheet. A circular disk graduated in degrees was attached to the rotor shaft and videotaped from above, with the resulting image mixed into a window on the flow image, providing an indication of the instantaneous value of rotor azimuth for each image. The delay between the actual and indicated azimuth values was calibrated by noting the indicated azimuth on frames, which showed different portions of the blade leading edge passing through the laser sheet. Averaging of values calculated from 10 such frames determined the true azimuth to an uncertainty of less than 0.5 deg.

Smoke from decomposing wax, generated by heating several vertical wax-coated wires upstream, was used as seeding in the flow. Given the short pulse duration, the low light intensity, and the uncertainty in the quality of seeding in the field of view at the instant of interest, the probability of obtaining clear images with seeding in the desired locations was not high. The images presented here are the best we were able to locate after considerable searching of the videotapes. However, the phenomena presented do occur repeatedly, so that they are not random smoke patterns.

The initiation of the secondary region is evident in the experimental results at around $\psi = 36$ deg. For these visualization results, the rotor speed was 1050 rpm, which results in a Reynolds number based on cylinder radius (0.067 m) of $Re = 1.5 \times 10^5$. Figure 8 shows vortex cross-sectional images captured at $\psi = 36$ and 42 deg with the laser sheet in the vertical plane $\theta = 90$ deg. The core of the tip vortex is discernible as the darkened portion at the center of the swirling fluid around it. The vortex core is designated by an arrow. Just under the vortex we see a lifting up of streamlines very near the wall (arrow), which is similar to the behavior of the computed

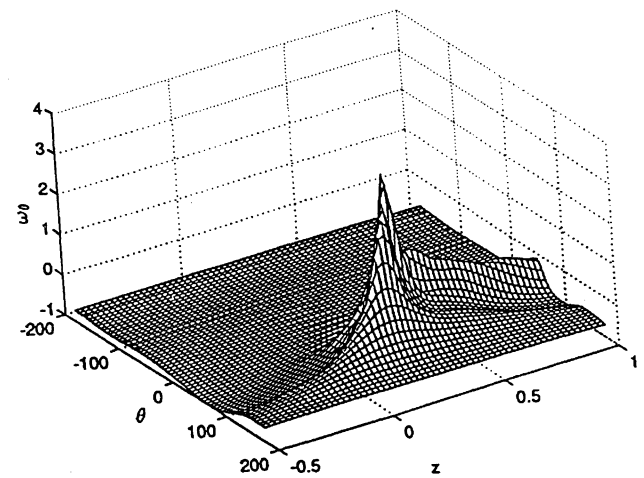

a) y = 0.5, maximum value ω_θ = 4.0

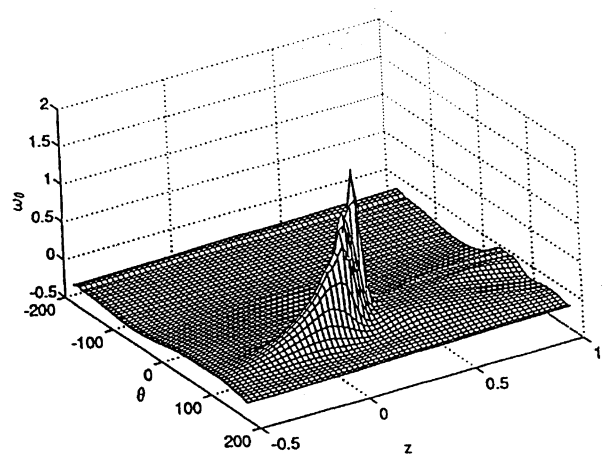

b) y = 1.2, maximum value ω_θ = 2.0

Fig. 7 Three-dimensional azimuthal vorticity component at different y positions.

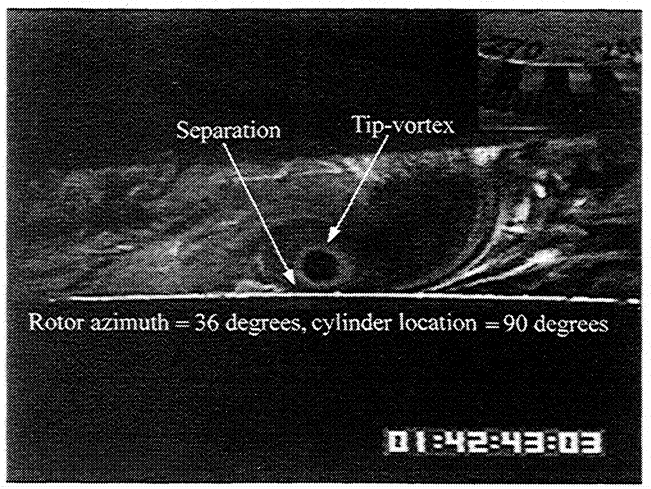

Fig. 8a Vortex cross-section image at ψ = 36 deg in the plane θ = 90 deg.

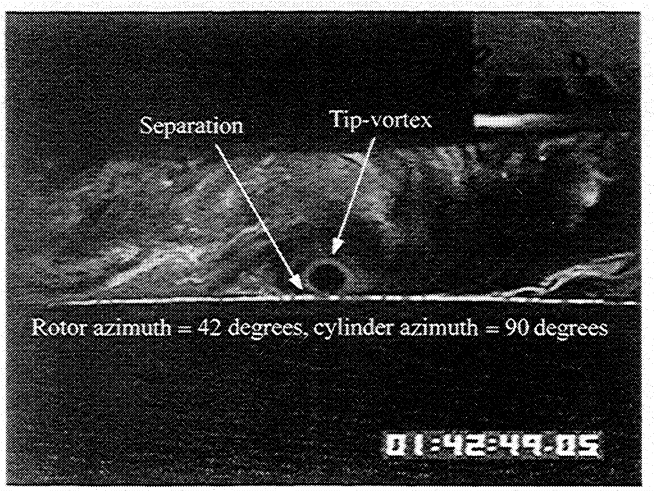

Fig. 8b Vortex cross-section image at ψ = 42 deg in the plane θ = 90 deg.

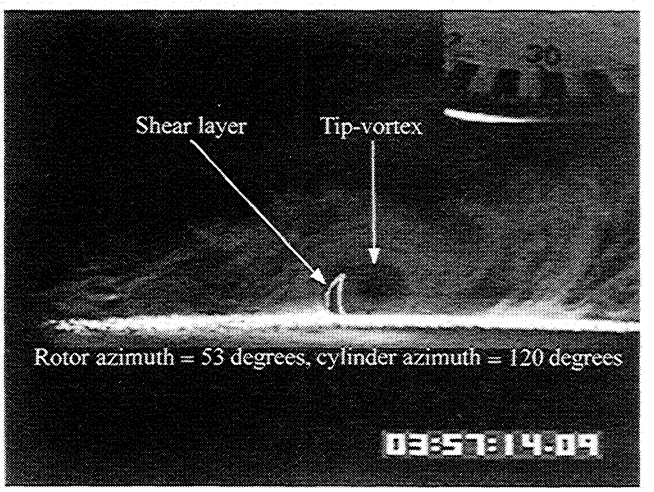

Fig. 9 Vortex cross-section image at ψ = 53 deg in the plane θ = 120 deg, which is on the retreating side of the rotor; retreating side is indicated in Fig. 2a.

streamline patterns shown in Fig. 4. The emergence of the separated region begins as a region of reduced velocity, which allows smoke to accumulate there (arrow).

For a larger value of ψ (Fig. 9), the velocities rise in magnitude, the local vorticity field intensifies, and the smoke will vacate the area leaving a void of high-vorticity, which in appearance resembles the vortex core region seen in the figure. Figure 9 shows results at $\psi = 53$ deg in a plane 30 deg from the vertical on the retreating side of the rotor ($\theta = 120$ deg). Note the darkened region just upstream of the vortex; this is believed to be a region of high-vorticity fluid indicating the development of a shear layer region as fluid is squeezed under the action of the very large adverse pressure gradient. Also, note that the secondary vortex and the main vortex are in the same relative position as in the earlier times shown in Fig. 8.

In Fig. 8a, the vortex core radius is about 6 mm and the vertical scale of the secondary flow is about 3 mm. At this time, the boundary-layer thickness estimated from the Reynolds number based on forward flight speed and the airframe radius is about 1–5 mm so that the vertical scale of the eruptive region is nominally about half the boundary-layer thickness indicating a mechanism whereby boundary-layer fluid may erupt into the mainstream.[10,18–20] In Fig. 2, the vertical extent of the separation region is about 1.5 mm at $\psi = 30$ deg, and this is consistent with the experimental result quoted earlier for $\psi = 36$ deg. Moreover, in Fig. 8a, the separation region begins about 12 mm upstream of the center of the vortex core, and converting to dimensional parameters, the results of Fig. 4 suggest that the separation region in the computations begins about 13 mm upstream (for $Re = 10^4$), which again is close to the experimental value.

Note that the rotor tip speed used to produce the results of Figs. 8 and 9 is half of that used to produce the other results described here (1050 rpm); this was done to facilitate visualization of the boundary-layer evolution. However, it can be shown using dimensional analysis that the dimensionless strength of the vortex remains the same in each case, which means that in the limit of infinite Reynolds number, the boundary-layer flows are equivalent. To show this, it is necessary to note that for both values of the rotor tip speed, the advance ratio defined as $\mu = W_\infty / \Omega R$, where $R = 0.457$ m is the rotor radius, remains fixed. At constant advance ratio, the value of the axial flow speed W_∞ for 2100 rpm is twice the value at 1050 rpm. However, from the work of McAlister et al.,[21] the swirl velocity and, hence, the dimensional circulation scale linearly with rotor speed, and so from Eq. (4), the dimensionless circulations are the same in both cases.

VI. Conclusions

In this work the viscous flow on the airframe due to a tip vortex shed from a helicopter airframe has been considered both computationally and experimentally. The early stages of the development of the secondary eddy in the boundary layer under the main tip vortex have been captured both computationally and experimentally. The experimental results support the computational results and indicate the appearance of a secondary flow under the main vortex, which is clearly discernible in the experiments at $\psi = 36$ deg. The genesis of this secondary flow is indicated by the computations, which show a reversed flow region developing under the main vortex just prior to $\psi = 30$ deg; the vorticity in the reversed flow region is of a sign opposite to that of the main vortex and, in the computations, begins to increase rapidly just after $\psi = 30$ deg.

One feature seen in the experiments is that the secondary flow is much more visible on the retreating side of the rotor ($\theta = 120$ deg), where the vortex is farther from the airframe. As discussed in the results section, this is suggested by the evolution of the vorticity distribution and the behavior of the radial velocity at the edge of the boundary layer.

Moreover, the position of the secondary vortex in the early times is consistent with the results of the experiments at the relatively later times indicated. From the plots themselves, the axial location of the center of the secondary flow in the computations is about 3 mm upstream of the center of the main tip vortex position, whereas the experiments indicate about 6 mm.

As noted by Sheridan and Smith,[1] the present problem is only one of a number of interactions that occur on an operating helicopter. To increase performance, it is imperative that these interactions be addressed; however, the computational challenges are significant. The scale of the sharp pressure gradients that generate the deep suction peaks in the pressure distribution on the top of the airframe are short in both space and time; this feature of the flow suggests that a purely computational approach to the present problem is likely to

fail. Consider, for example, in the present problem, a Navier–Stokes computation in which there are 200 points in each of the three coordinate directions; for simplicity, consider a Cartesian coordinate system. Suppose that the computation is to be based on the Georgia Institute of Technology configuration and that the total computational domain is based on the lengths $L_x = L_z = 2R + \Delta R$, where R is the rotor radius $R = 0.457$ m, $\Delta R = 0.36R$, and $L_y = 2H + H + D_{\text{airframe}} + 2H = 0.82$ m, where H is the rotor to airframe gap and is about 0.14 m. The diameter of the airframe is 0.134 m. Then the grid sizes are $\Delta x = \Delta z = 0.00625$ m and $\Delta y = 0.004$ m. As already discussed, a typical vortex radius is about 0.3 in. = 0.0076 m and the boundary-layer thickness is about 0.002 m based on the airframe radius and axial speed W_∞. Thus, in the present hypothetical computation, there would be no points within the boundary layer where separation begins and only one grid point to represent the vortex core. Moreover, because the three velocity components and the pressure need to be computed, for the present number of grid points, a minimum of 32×10^6 words of memory are required for a single time step. This is about the size of the typically available memory in a standard supercomputer, for example, Cray YMP, calculation. Clearly, under this situation it would be difficult to resolve the Navier–Stokes equations on these length scales; this is why the boundary-layer equations have been used here. An alternative approach is to use an adaptive grid Navier–Stokes solver, and this is under investigation.

Acknowledgments

The computational work described here has been supported by the U.S. Army Research Office under Contract DAAL03-K-0095. The experimental work is supported by the U.S. Army Research Office under Task 2 of the Center of Excellence in Rotary Wing Aircraft Technology. The continued support of the Contract Monitor of both these efforts, Thomas L. Doligalski, is greatly appreciated. The authors gratefully acknowledge the assistance of S.-G. Liou in the laser sheet flow visualization. The computations have been performed through a grant of computer time from Ohio Supercomputer Center.

References

[1]Sheridan, P. F., and Smith, R. F., "Interactional Aerodynamics—A New Challenge to Helicopter Technology," *Journal of the American Helicopter Society*, Vol. 25, No. 1, 1980, pp. 3–21.

[2]Affes, H., and Conlisk, A. T., "A Model for Rotor Tip Vortex–Airframe Interaction, Part 1: Theory," *AIAA Journal*, Vol. 31, No. 12, 1993, pp. 2263–2273.

[3]Affes, H., Conlisk, A. T., Kim, J. M., and Komerath, N. M., "A Model for Rotor Tip Vortex–Airframe Interaction, Part 2: Comparison with Experiment," *AIAA Journal*, Vol. 31, No. 12, 1993, pp. 2274–2282.

[4]Liou, S. G., Komerath, N. M., and McMahon, H. M., "Measurement of the Interaction Between a Rotor Tip Vortex and a Cylinder," *AIAA Journal*, Vol. 28, No. 6, 1990, pp. 975–981.

[5]Affes, H., Xiao, Z., and Conlisk, A. T., "The Boundary Layer Flow Due to a Vortex Approaching a Cylinder," *Journal of Fluid Mechanics*, Vol. 275, Sept. 1994, pp. 33–58.

[6]Brand, A. G., McMahon, H. M., and Komerath, N. M., "Correlations of Rotor/Wake-Airframe Interaction Measurements with Flow Visualization Data," *Annual Forum Proceedings*, American Helicopter Society, Vol. 2, 1990, pp. 1135–1143.

[7]Brand, A. G., "An Experimental Investigation of the Interaction Between a Model Rotor and Airframe in Forward Flight," Ph.D. Thesis, School of Aerospace Engineering, Georgia Inst. of Technology, Atlanta, GA, June 1989.

[8]Affes, H., "Tip-Vortex-Airframe Interactions," Ph.D. Thesis, Dept. of Mechanical Engineering, Ohio State Univ., Columbus, OH, June 1992.

[9]Harvey, J. K., and Perry, F. J., "Flowfield Produced by Trailing Vortices in the Vicinity of the Ground," *AIAA Journal*, Vol. 9, No. 8, 1971, pp. 1659, 1660.

[10]Walker, J. D. A., Smith, C. R., Cerra, A. W., and Doligalski, T. L., "The Impact of a Vortex Ring on a Wall," *Journal of Fluid Mechanics*, Vol. 181, Aug. 1987, pp. 99–140.

[11]Ersoy, S., and Walker, J. D. A., "The Viscous Flow Induced near the Wall by Counter-Rotating Vortex Pairs and Vortex Loops," Rept. FM-8, Lehigh Univ., Bethlehem, PA, June 1985.

[12]Hon, T. L., and Walker, J. D. A., "An Analysis of the Motion and the Effects of Hairpin Vortices," Rept. FM-11, Lehigh Univ., Bethlehem, PA, May 1987.

[13]Batchelor, G. K., *An Introduction to Fluid Dynamics*, Cambridge Univ. Press, Cambridge, England, UK, 1967, p. 95.

[14]Moore, D. W., "Finite Amplitude Waves on Aircraft Trailing Vortices," *Aeronautical Quarterly*, Vol. 23, 1972, pp. 307–314.

[15]Affes, H., and Conlisk, A. T., "The Three-Dimensional Boundary Layer Flow Due to a Vortex Filament Outside a Circular Cylinder," AIAA Paper 93-0212, Jan. 1993.

[16]Elliott, J. W., Cowley, S. J., and Smith, F. T., "Breakdown of Boundary Layers: i. On Moving Surfaces, ii. In Semi-Similar Flow, iii. In Fully Unsteady Flow," *Geophys. Astrophys. Fluid Dyn.*, Vol. 25, 1983, pp. 77–138.

[17]Van Dommelen, L., and Cowley, S. J., "On the Lagrangian Description of Unsteady Separation. Part 1. General Theory," *Journal of Fluid Mechanics*, Vol. 210, Jan. 1990, pp. 593–626.

[18]Affes, H., Xiao, Z., Conlisk, A. T., Kim, J. M., and Komerath, N. M., "The Three-Dimensional Boundary Layer Flow Due to a Rotor Tip Vortex," AIAA Paper 93-3081, July 1993.

[19]Chuang, F. S., and Conlisk, A. T., "The Effect of Interaction on the Boundary Layer Induced by a Convected Rectilinear Vortex," *Journal of Fluid Mechanics*, Vol. 200, March 1989, pp. 337–365.

[20]Doligalski, T. L., and Walker, J. D. A., "The Boundary Layer Induced by a Convected Rectilinear Vortex," *Journal of Fluid Mechanics*, Vol. 139, Feb. 1984, pp. 1–30.

[21]McAlister, K. W., Schuler, C. A., Branum, L., and Wu, J. C., "3-D Measurements near a Hovering Rotor for Determining Profile and Induced Drag," NASA TP 3577, Aug. 1995.

S. Fleeter
Associate Editor